Mon. Not. R. Astron. Soc. **000**, 000–000 (0000) Printed 28 February 2014 (MN LATEX style file v2.2)

In hot bubble: why superbubble feedback works and isolated supernovae do not?

Prateek Sharma[1] ⋆, Arpita Roy[1,2], Biman B. Nath[2], Yuri Shchekinov[3]
[1] *Joint Astronomy Programme and Department of Physics, Indian Institute of Science, Bangalore 560012, India*
[2] *Raman Research Institute, Sadashiva Nagar, Bangalore 560080, India*
[3] *Department of Physics, Southern Federal University, Rostov on Don 344090, Russia*

arXiv:1402.6695v1 [astro-ph.GA] 26 Feb 2014

28 February 2014

ABSTRACT

Most massive stars form in star clusters extending over just few 10s of pc. Fast winds from massive stars and the first supernovae are expected to create a hot, dilute bubble which encompasses the whole star cluster. Thus subsequent supernovae go off in a dilute, non-radiative bubble and power a superwind. Continuous energy injection via successive supernovae going off within the hot bubble maintains a strong termination shock, which keeps the superbubble over-pressured and drives the outer shock well after it becomes radiative. Isolated supernovae, in contrast, do not have further energy injection, become radiative quite early ($\lesssim 0.1$ Myr, 10s of pc), and stall at scales $\lesssim 100$ pc because of radiative and adiabatic losses. While isolated supernovae lose almost all of their mechanical energy by a Myr, superbubbles can retain up to $\sim 40\%$ of the input energy in form of mechanical energy over the lifetime of the star cluster (few 10s of Myr). Thus, superbubbles are expected to be more effective feedback agents compared to isolated supernovae. These conclusions are likely to hold even in presence of realistic magnetic fields and thermal conduction.

We compare various recipes for implementing supernova feedback in numerical simulations. We show that the supernova energy needs to be deposited over a small volume in order for it to couple to the ISM. We stress upon the importance of thermalization of supernova energy, which forms the basis of our analytic estimates. We verify our analytic scalings with numerical simulations. Individual supernova ejecta needs to thermalize within the termination shock for the appearance of a simple Chevalier & Clegg (CC85) thermal wind within the hot bubble. A steady thermal wind appears only for a large number ($\gtrsim 10^4$) of supernovae. For smaller clusters we expect multiple internal shocks instead of a smooth, dense thermalized CC85 wind.

Key words: galaxies: ISM – ISM: bubbles – shock waves – supernova remnants

1 INTRODUCTION

Gravity and dark energy govern the structure in the universe at the largest scales but complex hydrodynamic processes like cooling, heating, self gravity and star formation are important at galactic scales (e.g., Springel et al. 2005). Numerical simulations have made tremendous progress in understanding galaxy formation, starting from pure gravitational N-body simulations to the current models which try to model the aforementioned complex processes. Modeling gravity is straightforward in principle, and only limited by the available computing power. But the modeling of hydrodynamic processes is rather involved. In particular, there is no consensus on which hydrodynamic processes are important and how they should be implemented numerically. Given the dynamic range of scales, from large scale structure (10s of Mpc)

⋆ prateek@physics.iisc.ernet.in

© 0000 RAS

to an individual star forming cloud (∼pc), simulations have to resort to unresolved 'subgrid' models for star formation and feedback due to star formation (e.g., Navarro & White 1993; Gerritsen 1997; Springel & Hernquist 2003; Guedes et al. 2011; Hopkins, Quataert, & Murray 2012 and references therein). While different star formation recipes seem to give similar star formation histories and stellar mass distributions, provided molecular clouds are resolved (e.g., Hopkins, Quataert, & Murray 2011), simulations are quite sensitive to the various feedback prescriptions (e.g., thermal feedback due to supernovae, momentum injection via dust absorbing/scattering photons produced by massive stars and supernovae) even with high resolution.

Stars form in clusters and super star clusters (100s to 10^6 stars) of various sizes and in different environments, ranging from low density galactic outskirts to dense galactic centers (see Protegies Zwart et al. 2010 for a review). These clusters are observed to disrupt the dense molecular clouds in which they are born (e.g., see Leisawitz et al. 1989; Zhang et al. 2001). This stellar feedback (due to strong radiation, stellar winds and supernovae) disperses cold gas and suppresses further star formation. Because of the stellar initial mass function (IMF) and the main sequence lifetimes, the energy input is roughly constant per unit time over the life time of stars more massive than $8M_\odot$ ($\sim$ 50 Myr; McCray & Kafatos 1987). Therefore, stellar feedback is sometimes modeled as a constant luminosity driven blast wave (Weaver et al. 1977; Mac Low, McCray, & Norman 1989; Gerritsen 1997). A superbubble (SB) expands faster than an isolated supernova remnant (SNR) because of continuous energy injection, and suffers smaller cooling losses because most supernovae (SNe) go off in a low density bubble.

The hot bubble breaks out through the gas disk if the outer shock driven by overlapping SNe crosses the scale height with a sufficient Mach number within the starburst lifetime (e.g., see section 2 of Roy et al. 2013). After breakout the hot, metal-rich stellar ejecta is spread out into the galactic halo via the Rayleigh-Taylor instability. Spreading of metals over large scales is required to explain the high metallicity observed in the intergalactic medium (IGM), far away from the stellar disk (Tumlinson et al. 2011).

Standard models for feedback through multiple SNe assume that a fraction $\gtrsim 0.3$ of the total explosion energy is retained in the hot ISM (e.g., Strickland & Heckman 2009). This fraction is much larger than the estimates for a single SNR (~ 0.1) after the radiative phase at $\lesssim 0.1$ Myr (e.g., Cox 1972; Chevalier 1974; Thornton et al. 1998). Moreover, there are further radiative and adiabatic losses, such that over the timescale of order tens of Myr, the available mechanical energy in the bubble and shell is a negligible ($\ll 0.1$) fraction of the initial supernova (SN) energy input. Recently Nath & Shchekinov (2013) argued that SBs created by multiple SNe in a star cluster are more effective as a feedback mechanism, in comparison to incoherent SNe. Recent simulations of interacting SNe by Vasiliev et al. 2014 show that the fractional energy retained as thermal energy in the hot ISM can be as large as $\sim$ 0.1–0.3 only if the explosions are spatially and temporally correlated such that the radiative losses are effectively compensated by new explosions. SBs produced by compact star clusters are expected to satisfy this condition. In this paper we assume all SNe to be coincident, a good approximation if the SNR, when it becomes radiative, encompasses the whole cluster. This makes SBs a more effective feedback agent which is responsible for magnificent galactic outflows.

In addition to elucidating differences between isolated SNe and SBs, we compare various methods of injecting SN energy in numerical simulations of the ISM. Different feedback processes, such as radiation pressure, photoionization, and cosmic rays, are important in explaining outflows in galaxies of different masses and redshifts (e.g., Hopkins, Quataert, & Murray 2012 and references therein). In this paper we only focus on the most important feedback component, thermal feedback due to SNe. We find that the SN thermal energy must be deposited over a sufficiently small volume for it to create a hot bubble and to have an impact on the surroundings. For a large energy deposition radius the cooling time is shorter than the thermalization timescale and thermal feedback is artificially suppressed. Most early implementations of SN feedback suffered from this problem (see Gerritsen 1997 and references therein).

The formation of a low density bubble is essential for thermal SN feedback to work because the energy of subsequent SNe is deposited in the low density bubble and is not radiated instantaneously; cooling is only restricted to the outer shock. While this fact has been appreciated (e.g., Gnedin 1998; Joung & Mac Low 2006), we present *quantitative* conditions for the formation of a strong shock and a hot, dilute bubble for different thermal feedback prescriptions. The main culprit responsible for the inefficacy of thermal feedback, in both Eulerian (e.g., Tasker & Bryan 2006; Dubois & Teyssier 2008) and Lagrangian (Springel & Hernquist 2003; Stinson et al. 2006) simulations, is the lack of resolution. In reality, a SN affects its surroundings starting at small ($\ll 1$ pc) scales by launching very fast ejecta ($\sim 10^4$ km s^{-1}) into the ISM (e.g., see Chevalier 1977). Simulations in which SN energy is not deposited at small enough scales have to resort to artificial measures (turning off cooling for several energy injection timescales, depositing energy into artificial 'hot' phase that does not cool, etc.) in order for feedback to have any impact at all on the ISM.

The continuous injection of mass and energy by SNe deep within the hot SB is expected to launch a steady wind (as first calculated by Chevalier & Clegg (1985); hereafter CC85). CC85 obtained analytic solutions for a superwind assuming a constant thermal energy and mass input rate with an injection radius. By modeling realistic SNe as fast moving ejecta within SBs we show that a steady CC85 wind is obtained only if a large number of SNe ($\gtrsim 10^4$) go off within the star cluster. For a smaller number of SNe their kinetic energy is not thermalized within a small injection radius and there is no steady outflow. This should have implications for works that simply assume a CC85 wind within the SB.

The paper is organized as follows. In section 2 we describe various ways of implementing thermal feedback due to SNe.

In section 3 we present different analytic criteria for feedback to work with different numerical prescriptions. We also derive the conditions for obtaining a thermalized CC85 wind within a SB. In section 4 we present 1-D numerical simulations of different feedback recipes with and without cooling, and compare the results with our analytic estimates. We show that radiative losses for isolated SNRs are much larger than SBs. We also briefly discuss the effects of magnetic fields and thermal conduction. In section 5 we discuss the implications of our results on galaxy formation, feedback simulations, and on galactic wind observations.

2 ISM & SN FEEDBACK PRESCRIPTIONS

Although ISM is multiphase and extremely complex, for simplicity we consider a uniform, static model with a given density (typically $n = 1$ cm^{-3}) and temperature (10^4 K corresponding to the warm ISM). We do not consider stratification because the disk scale height is typically a few 100 pc and the fizzling of SN feedback is essentially a small scale problem. Once a bubble is formed within a scale height, it will break out of the disk if the outer shock crosses the scale height with a sufficiently large Mach number; isolated SNe for typical ISM parameters are unable to break out and affect the large scale inflows. For simplicity we also assume that all SNe explode at $r = 0$. This is a good approximation because the size of a typical star cluster is smaller than the bubble size in the radiative phase.

Various SN prescriptions we consider in our numerical simulations, corresponding to most thermal SN feedback models in the literature, are:

(i) *Kinetic Explosion Models* (KE): In these models the SN energy ($E_{\rm ej}$, chosen to be 1 Bethe $\equiv 10^{51}$ erg) is given to a specified ejecta mass ($M_{\rm ej}$, chosen to be 1 $M_\odot$) distributed uniformly with an ejecta density $\rho_{\rm ej} = 3M_{\rm ej}/[4\pi r_{\rm ej}^3]$ within an ejecta radius $r_{\rm ej}$. The ejecta velocity is homologous with $v_{\rm ej}(r) = v_0(r/r_{\rm ej})$ within the ejecta; the normalization is such that the kinetic energy of the ejecta is $E_{\rm ej}$; i.e., $v_0 = (10E_{\rm ej}/3M_{\rm ej})^{1/2}$. The ejecta temperature is taken to be small ($T_{\rm ej} = 10^4$ K). After every (fixed) SN injection time $t_{\rm SN}$ the innermost $r_{\rm ej}$ of the volume is *overwritten* by the ejecta density and velocity, thereby pumping SN energy into the ISM. After the reverse shock propagates toward the bubble center, once the swept-up mass is comparable to the ejecta mass, the bubble density structure is fairly insensitive to the ejecta density distribution (Truelove & McKee 1999). This model most closely resembles a physical SNR in early stages at small ($\ll 1$ pc) scales when the SN 'piston' at large speed rams into the ISM. Because of its computational expense this prescription is not widely used in galaxy formation simulations (there are some exceptions, e.g., Tang & Wang 2005).

(ii) *Thermal Explosion Models* (TE): In these models the energy is deposited within the ejecta radius in form of thermal energy at an interval of $t_{\rm SN}$. There are two variants of this model. In one class, the mass and internal energy densities are *overwritten* within the ejecta radius ($r_{\rm ej}$) such that the *uniformly distributed* ejecta thermal energy is $E_{\rm ej}$ (1 Bethe) and the *uniformly distributed* ejecta mass is $M_{\rm ej}$ ($1M_\odot$). We abbreviate these models as TEo and they behave like KE models. The second class of models is where we *add* (in contrast to overwrite) the ejecta mass (with uniform density) to the preexisting mass and the ejecta thermal energy (distributed uniformly) to the preexisting internal energy within $r_{\rm ej}$. We refer to these models as TEa. There are significant differences between the TEa and TEo/KE models in presence of cooling because TEa ejecta can become radiative if thermal energy is added to a dense ISM. Most models in the literature are analogous to TEa models with some variations (e.g., Katz 1992, Joung & Mac Low 2006, Creasey, Theuns, & Bower 2013; some works such as Stinson et al. 2006 ,Thacker & Couchman 2000, Agertz, Teyssier, & Moore 2011 unphysically turn off cooling for some time for SN feedback to have an impact). Sometimes all the SN energy is deposited in a single grid cell (e.g., Tasker & Bryan 2006) or in a single particle (e.g., SN particle method in section 3.2.4 of Gerritsen 1997).

(iii) *Luminosity Driven Models* (LD): As discussed earlier, for typical IMFs, the mechanical energy input due to OB stars per unit time is roughly constant. This motivates a model in which internal energy and mass within an injection radius (denoted by $r_{\rm ej}$) increase at a constant rate corresponding to internal energy $E_{\rm ej}$ and mass $M_{\rm ej}$ for each SN. Some of the works that use this prescription are Chevalier & Clegg 1985; Mac Low, McCray, & Norman 1989; Suchkov et al. 1994; Mac Low & Ferrara 1999; Strickland & Stevens 2000; Cooper et al. 2008; Roy et al. 2013; Recchi & Hensler 2013; Palouš et al. 2013.

All our models are identified with the number of OB stars $N_{\rm OB}$ (which equals the number of SNe in the star cluster) or luminosity $L_{\rm ej} = E_{\rm ej}/t_{\rm SN} = N_{\rm OB}E_{\rm ej}/t_{\rm OB}$, where $t_{\rm OB}$ is the lifetime of the OB association (taken to be 30 Myr) and $t_{\rm SN} = t_{\rm OB}/N_{\rm OB}$ is the time interval between SNe.

3 ANALYTIC CRITERIA

In this section we present the analytic criteria that need to be satisfied for various feedback models discussed in section 2 to work. While radiative cooling is the most discussed phenomenon in the context of fizzling SN feedback, the feedback prescription should satisfy additional constraints for the energy input to couple realistically with the ISM. A recurring concept in what follows is that of thermalization; i.e., in order to be effective the input energy should have time to couple to the ISM before it is radiated or is overwritten. In section 3.3 we show that a steady superwind within a superbubble, as envisaged by Chevalier & Clegg (1985), occurs only if the number of SNe is sufficiently large.

3.1 Energy coupling without cooling

3.1.1 Ejecta radius constraint for overwrite models

In models where energy within the ejecta radius is overwritten (KE, TEo) the ejecta radius should be smaller than a critical radius ($r_{\rm ej} \lesssim r_{\rm crit}$) for the input energy to get coupled to the ISM. The critical radius equals the Sedov-Taylor shock radius at $t_{\rm SN}$,[1] the time lag between SNe,

$$r_{\rm crit} \equiv \left(\frac{E_{\rm ej} t_{\rm SN}^2}{\rho}\right)^{1/5} \approx 50 \text{ pc } n^{-1/5} E_{\rm ej,51}^{1/5} t_{\rm SN,0.3}^{2/5}, \quad (1)$$

where ρ (n) is the ISM (number) density (assuming $\mu = 0.62$), $E_{\rm ej,51}$ is the ejecta energy in units of 10^{51} erg, and $t_{\rm SN,0.3}$ is the time between consecutive SNe in units of 0.3 Myr. If the ejecta radius is larger than this value the ejecta energy is overwritten before it can push the outer shock. Thus, in such a case, the input SN energy is overwritten without much affecting the ISM.

3.1.2 Sonic constraint

For thermal SN feedback to launch a strong shock the energy should be deposited over a small enough volume, such that the post-shock pressure is much larger than the ISM pressure. This is equivalent to demanding the outer shock velocity to be much larger than the sound speed in the ISM. The shock velocity ($v_{\rm OS} \equiv dr_{\rm OS}/dt$; $r_{\rm OS}$ is the outer shock radius), expressed in terms of the shock radius in Sedov-Taylor stage, is $v_{\rm OS} \approx 0.4 E_{\rm ej}^{1/2} \rho^{-1/2} r_{\rm OS}^{-3/2}$ for an isolated SN and $v_{\rm OS} \approx 0.6 L_{\rm ej}^{1/3} \rho^{-1/3} r_{\rm OS}^{-2/3}$ for a luminosity driven SB (Weaver et al. 1977). The condition for a strong shock for an isolated SN is ($v_{\rm OS} \lesssim a_T$; a_T is the ISM isothermal sound speed)

$$r_{\rm ej} \lesssim 174 \text{ pc } E_{\rm ej,51}^{1/3} n^{-1/3} T_4^{-1/3} \quad (2)$$

and for a SB is (see Eq. 3 in Silich et al. 2009)

$$r_{\rm ej} \lesssim 1.5 \text{ kpc } L_{\rm ej,38}^{1/2} n^{-1/2} T_4^{-3/4}, \quad (3)$$

where $L_{\rm ej,38}$ is the ejecta luminosity ($L_{\rm ej} = E_{\rm ej}/t_{\rm SN}$ for explosion models) in units of 10^{38} erg s^{-1} (this corresponds to $N_{\rm OB} = 100$ over $t_{\rm OB} = 30$ Myr) and T_4 is the ISM temperature in units of 10^4 K.

The sonic constraint ($v_{\rm OS} \lesssim a_T$) is typically less restrictive than the compactness requirements due to cooling in a dense ISM (see next section). Tang & Wang (2005), who considered supernova feedback in the hot ISM ($\sim 10^7$ K) of galaxy clusters and elliptical galaxies, found that the shock can quickly (when outer radius is only ≈ 20 pc; see Eq. 2) decelerate to attain the sound speed in the hot ISM. After this the outer shock propagates as a sound wave. While the sound wave can spread the SN energy over a larger radius ($\propto t$ for a sound wave, unlike a strong blast wave in which $r_{\rm OS} \propto t^{2/5}$), unlike in shocks, the energy in the sound wave is not dissipated efficiently.

[1] We use the Sedov-Taylor expression for the bubble radius in Eq. 1 because the shock quickly transitions from a free-expanding to a Sedov-Taylor state; the Sedov-Taylor radius (when the swept up ISM mass equals the ejecta mass) is $r_{\rm ST} \equiv (3M_{\rm ej}/4\pi\rho)^{1/3} \approx 2.5 \text{ pc } M_{\rm ej,\odot}^{1/3} n^{-1/3}$, much smaller than the estimate in Eq. 1, where $M_{\rm ej,\odot}$ is the ejecta mass in solar units.

3.2 Energy coupling with cooling

3.2.1 Luminosity driven model

In luminosity driven models (LD) SN feedback does not fizzle out (in fact, the shock can get started) only if the cooling rate is smaller than the energy deposition rate, i.e., $3L_{\rm ej}/4\pi r_{\rm ej}^3 \gtrsim n^2\Lambda$ ($\Lambda[T]$ is the cooling function), or

$$r_{\rm ej} \lesssim 20 \text{ pc } L_{\rm ej,38}^{1/3} n^{-2/3} \Lambda_{-22}^{-1/3}, \quad (4)$$

where Λ_{-22} is the cooling function in units of 10^{-22} erg cm^3 s^{-1}.

3.2.2 Thermal explosion addition model

The above criterion (Eq. 4) for the luminosity driven models is quite different from the criterion that we now derive for the widely used thermal explosion models with energy and mass addition (TEa model in section 2). Since energy is *added* to the (possibly dense) pre-existing medium, cooling in this model can be substantial. In contrast, since the ejecta density is low, cooling losses are smaller in the overwriting models (KE, TEo). For TEa models to launch a shock, radiative losses over the timescale in which the shock from a point explosion reaches the ejecta radius,

$$t_{\rm ej} = E_{\rm ej}^{-1/2} r_{\rm ej}^{5/2} \rho^{1/2}, \quad (5)$$

should be smaller than the energy deposited; i.e.,

$$n^2 \Lambda t_{\rm ej} \lesssim 3E_{\rm ej}/4\pi r_{\rm ej}^3. \quad (6)$$

Plugging in the expression for $t_{\rm ej}$, we get

$$r_{\rm ej} \lesssim 31 \text{ pc } E_{\rm ej,51}^{3/11} \Lambda_{-22}^{-2/11} n^{-5/11}. \quad (7)$$

This condition is much more restrictive than the one obtained by replacing $t_{\rm ej}$ in Eq. 6 by the CFL stability timestep. Moreover, this is the appropriate timescale to use because the relevant timescale for the injected energy to couple to the ISM is the thermalization time ($t_{\rm ej}$).

3.2.3 Overwrite models

In models where the energy and mass densities are overwritten within $r_{\rm ej}$, the condition for overcoming cooling losses and launching a shock is

$$n_{\rm ej}^2 \Lambda t_{\rm ej} \lesssim \frac{3E_{\rm ej}}{4\pi r_{\rm ej}^3},$$

where ejecta number density $n_{\rm ej} = \rho_{\rm ej}/\mu m_p$ and $\rho_{\rm ej} = 3M_{\rm ej}/4\pi r_{\rm ej}^3$; note that this expression is different from Eq. 6 in that the ejecta density is used instead of the ISM density. The overwrite models (KE, TEo) behave quite differently

from addition (TEa, LD) models because a larger ejecta radius means a smaller density ejecta to which energy is added. Replacing the ISM density by the ejecta density in Eq. 5 gives $t_{\rm ej} = E_{\rm ej}^{-1/2} r_{\rm ej}^{5/2} \rho_{\rm ej}^{1/2}$, and the condition for energy thermalization is

$$r_{\rm ej} \gtrsim 0.003 \text{ pc } M_{\rm ej,\odot}^{5/4} \Lambda_{-22}^{1/2} E_{\rm ej,51}^{-3/4}. \quad (8)$$

In order to avoid radiative losses the ejecta radius should be *larger* than above. This early cooling of the mass loaded SN ejecta, responsible for creating cold filaments in young SNe (e.g., Chevalier & Blondin 1995), is physical (unlike fizzling out of energy addition models) and should reduce the energy available to drive the SN. All our simulations use an ejecta radius much greater than this limit.

3.3 Conditions for CC85 wind

Chevalier & Clegg 1985 (hereafter CC85) found analytic solutions for a luminosity driven wind with a fixed injection radius. Luminosity injection is expected to drive both an outer shock bounding the bubble and a wind that shocks within the hot bubble at the termination shock (see Fig. 1 in Weaver et al. 1977). In this section we show that for a small number of SNe (c.f. Eq. 11) the SN ejecta does not thermalize within the termination shock. The density inside the bubble is much lower than the CC85 wind because most SNe occur in the dilute bubble created by earlier SNe and the thermalization radius is comparable to the outer shock radius. This has important implications on cooling and luminosity of SN ejecta.

Following Weaver et al. (1977), the outer shock radius of a luminosity driven bubble is given by $r_{\rm OS} \approx (L_{\rm ej} t^3/\rho)^{1/5}$, velocity by $v_{\rm OS} \approx 0.6 r_{\rm OS}/t \propto t^{-2/5}$, and the post-shock pressure by $p_{OS} \approx 0.75 \rho v_{\rm OS}^2 \approx 0.27 L_{\rm ej}^{2/5} \rho^{3/5} t^{-4/5}$. Assuming a steady superwind, the ram pressure at the termination shock ($r_{\rm TS}$; the wind is assumed to be supersonic at this radius) is $\rho_{\rm TS} v_{\rm TS}^2 = \dot{M}_{\rm ej} v_{\rm TS}/(4\pi r_{\rm TS}^2)$, where $v_{\rm TS} = (2L_{\rm ej}/\dot{M}_{\rm ej})^{1/2}$ is the wind velocity, $\rho_{\rm TS}$ is the density upstream of the termination shock, and $\dot{M}_{\rm ej}$ is the mass injection rate. The wind termination shock ($r_{\rm TS}$) is located where the wind ram pressure balances the bubble pressure; i.e.,

$$\frac{\dot{M}_{\rm ej} v_{\rm TS}}{4\pi r_{\rm TS}^2} \approx 0.75 \rho v_{\rm OS}^2.$$

Using $v_{\rm OS} \approx 0.6 L_{\rm ej}^{1/3} \rho^{-1/3} r_{\rm OS}^{-2/3}$ and $\dot{M}_{\rm ej} = 2L_{\rm ej}/v_{\rm TS}^2$ gives,

$$\frac{r_{\rm TS}}{r_{\rm OS}} \approx \left(\frac{v_{\rm OS}}{v_{\rm TS}}\right)^{1/2} \approx 0.08 E_{\rm ej,51}^{-1/12} M_{\rm ej,\odot}^{1/4} n^{-1/6} r_{\rm OS,2}^{-1/3} t_{\rm SN,0.3}^{-1/6}, \quad (9)$$

where $r_{\rm OS,2}$ is the outer shock radius in units of 100 pc, $t_{\rm SN,0.3}$ is the time between SNe normalized to 0.3 Myr (corresponding to $N_{\rm OB} = 100$); we have used $L_{\rm ej} = E_{\rm ej}/t_{\rm SN}$ and $\dot{M}_{\rm ej} = M_{\rm ej}/t_{\rm SN}$. The ratio $r_{\rm TS}/r_{\rm OS}$ depends very weakly on time ($\propto t^{-1/5}$); this comes from the time dependence of $r_{\rm OS}$ in Eq. 9. The reverse shock for an isolated SN very quickly (at the beginning of Sedov-Taylor stage) collapses to a point but the termination shock for a SB is present at all times. Thus the non-radiative termination shock can power a SB long after the outer shock becomes radiative, unlike a SN which dies off shortly after the outer shock becomes radiative (see section 4.5.4 for our results from simulations).

The condition for the existence of a smooth CC85 wind is that the ejecta thermalization radius should be smaller than the termination shock radius. The superwind is mass loaded by previous SNe (the bubble density in the absence of mass loading is quite small because most of the mass is swept up in the outer shell). The swept up mass till radius r in a CC85 wind is

$$M_{\rm sw} = \int_0^r 4\pi r'^2 \rho_w(r') dr' \approx \frac{\dot{M}_{\rm ej} r}{v_{\rm TS}} = \frac{M_{\rm ej} r}{t_{\rm SN} v_{\rm TS}},$$

where $\rho_w(r')$ is the wind density profile; here we have assumed that the swept up mass is dominated by the supersonic portion of the wind. Now the thermalization radius (the radius within which the deposited energy is thermalized and which should correspond to CC85's injection radius) of the ejecta is where the swept up mass roughly equals the ejecta mass, or

$$r_{\rm th} \approx v_{\rm TS} t_{\rm SN} \approx 3 \text{ kpc } E_{\rm ej,51}^{1/2} M_{\rm ej,\odot}^{-1/2} t_{\rm SN,0.3}. \quad (10)$$

Since the thermalization radius is quite large, a thermalized CC85 solution will only occur for large clusters (with shorter $t_{\rm SN}$, the time lag between SNe); for modest star clusters the ejecta will only thermalize beyond the termination shock. Of course, the thermalization radius cannot be smaller than the size of the star cluster launching the energetic ejecta. Using Eq. 9 and $r_{\rm OS} \approx (L_{\rm ej} t^3/\rho)^{1/5}$ the termination shock radius can be expressed as

$$r_{\rm TS} \approx 5 \text{ pc } E_{\rm ej,51}^{1/20} M_{\rm ej,\odot}^{1/4} n^{-3/10} t_{\rm SN,0.3}^{-3/10} t_{0.3}^{2/5},$$

where $t_{0.3}$ is time in units of 0.3 Myr. A CC85 solution will appear only if this termination shock radius is larger than the thermalization radius (Eq. 10); i.e.,

$$t_{\rm SN,0.3} \lesssim 0.007 E_{\rm ej,51}^{-9/26} t_{0.3}^{4/13} n^{-3/13} M_{\rm ej,\odot}^{15/26}. \quad (11)$$

This means that $N_{\rm OB} \gtrsim 3500$ (recall that $t_{\rm SN} = t_{\rm OB}/N_{\rm OB}$, where $t_{\rm OB} = 30$ Myr is the cluster lifetime and $N_{\rm OB}$ is the number of SNe) is required for a CC85 wind to appear by 30 Myr. Thus, a thermally driven CC85 wind occurs only for a sufficiently big starburst, with a large mass loading, and at late times.

4 SIMULATIONS & RESULTS

We study the most basic setup of an initially uniform, warm ISM (10^4 K; at scales of few 100 pc) around a super star cluster in which SNe deposit their energy at a single point. This simplification is justified because the scales of interest (100s of pc; few Myr) are much bigger than the cluster size and the local ISM/circumstellar inhomogeneities. We vary the ISM density and SN injection parameters to assess when SN energy can significantly affect the ISM, both with and without cooling. We also numerically verify the various analytic constraints presented in section 3.

4.1 Numerical setup

In this section we describe various one-dimensional numerical simulations based on models of section 2. The ISM density and temperature are chosen to 1 cm^{-3} and 10^4 K, respectively, unless specified otherwise. The mean mass per particle is $\mu = 0.62$ and per electron is $\mu_e = 1.17$. The initial density and temperature are uniform, and velocity is zero. SN feedback is implemented via one of the methods discussed in section 2.

We use the `ZEUS-MP` code in spherical, one-dimensional geometry (Hayes et al. 2006) to solve the standard Euler equations with source terms mimicking SN energy/momentum/mass injection for the chosen feedback model and a sink term in the internal energy equation representing radiative cooling (similar but not identical to Eqs. 20-22 in Roy et al. 2013). While most of our runs are hydro, in section 4.5.5 we briefly discuss runs with simple models of magnetic fields and thermal conduction.

Radial velocity is set to zero at the inner radial boundary and other fluid variables are copied in the ghost cells. Outer boundary is far away and out of causal contact. Since the setup produces strong shocks, we use the standard `ZEUS` artificial viscosity to prevent unphysical oscillations at shocks (Stone & Norman 1992). The CFL number of 0.2 is found to be more robust compared to the standard value of 0.5, and is used in all simulations. Cooling function is based on the solar metallicity table of Sutherland & Dopita (1993) with the cooling function set to zero below 10^4 K. The cooling step is implemented via operator splitting using the semi-implicit method of Sharma, Parrish, & Quataert (2010). Cooling is subcycled and the number of subcycles is limited to be less than 100.

Most of our runs use a 1024 resolution grid extending from 1 pc to 2 kpc. A logarithmically spaced grid is used to better resolve smaller radii. Some runs with stronger SN feedback use a larger spatial extent (c.f. $N_{\rm OB} = 10^6$ runs in Fig. 3), and some very high uniform resolution runs (16384 grid points; c.f. Fig. 5) use a smaller extent (1 to 200 pc). All our simulations are run for 30 Myr, typical age of a young star cluster.

4.2 Realistic SN shock (KE models)

The SN shock is launched once a protoneutron star forms at the center of a massive evolved star (with size $\sim 10^{14}$ cm). In the ejecta dominated state (before the swept up ISM mass is less than the ejecta mass) the cold ejecta is dominated by kinetic energy (e.g., Truelove & McKee 1999). In our 'realistic' simulations (KE models; see section 2) we choose the ejecta to have a constant density and a velocity proportional to the radius (homologous expansion; this is a similarity solution for the freely expanding ejecta) within the ejecta. The SN shock develops a reverse shock after sweeping up its own mass in the ISM; this slows down the ejecta and communicates the presence of the ISM to the supersonic ejecta. In this section we compare the evolution of *adiabatic* (cooling is turned off)

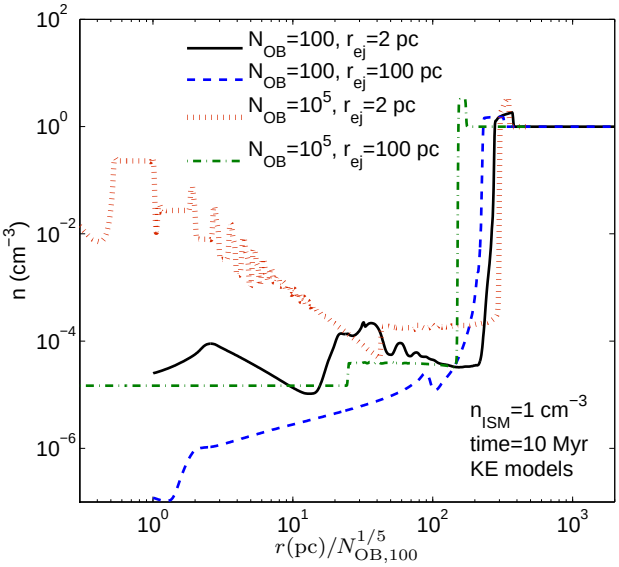

Figure 1. Number density as a function of radius (scaled to the self-similar scaling) for different parameters of realistic KE runs at 10 Myr. The outer shock is closer in for models using a larger ejecta radius because energy is overwritten before it can couple to the ISM.

KE models with different parameters, highlighting the importance of having a small ejecta radius ($r_{\rm ej}$) even in absence of cooling for overwrite (KE, TEo) models. We have verified that kinetic explosion (KE) and thermal explosion overwrite (TEo) models behave in a similar fashion.

Figure 1 shows the density profile as a function of radius (normalized to the self similar scaling, $r_{\rm OS} \approx [L_{\rm ej} t^3/\rho]^{1/5}$, where $L_{\rm ej} = E_{\rm ej}/t_{\rm SN} = E_{\rm ej} N_{\rm OB}/t_{\rm OB}$) for different realistic runs (results are similar for TEo models) with $N_{\rm OB} = 100,\ 10^5$ at 10 Myr. The runs with a large ejecta radius (100 pc) give a smaller outer shock radius because most of the energy is overwritten without being thermalized (see section 3.1.1 for a discussion). The problem is worse for larger $N_{\rm OB}$ (shorter $t_{\rm SN}$), as expected from Eq. 1. The normalized location of the outer shock falls almost on top of each other for a small ejecta radius ($r_{\rm ej} = 2$ pc) but the shock is weaker, broader, and with a modest density jump for a smaller number of SNe, as expected.

4.3 Comparison of adiabatic models

While the KE model is most realistic, we expect other models in section 2 to give a similar location for the outer shock after the swept-up ISM mass equals the ejecta mass, and the shock is in the Sedov-Taylor regime. The structure within the bubble depends on SN prescription, as we show in section 4.4.

Figure 2 shows the location of the outer shock (measured by it peak density) as a function of time for various models (KE, LD, TEa) and SN parameters in absence of cooling. The solid line at the bottom shows the transition from a sin-

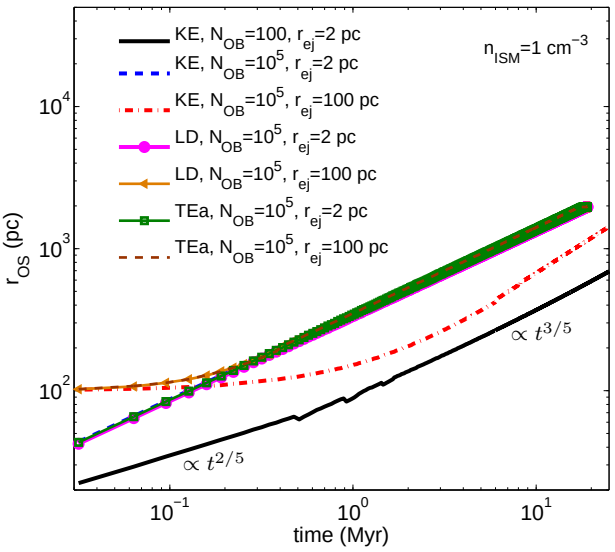

Figure 2. The outer shock radius as a function of time for various runs using kinetic explosion (KE), luminosity driven (LD) and thermal explosion addition (TEa) models. The KE models give correct results only if the ejecta radius ($r_{\rm ej}$) is sufficiently small because energy is overwritten before getting coupled to the ISM. There is no such problem for energy addition and luminosity driven models. At early times the outer shock radius scales with the Sedov-Taylor scaling ($r_{\rm OS} \propto t^{2/5}$) and later on, after many SNe go off, it steepens ($r_{\rm OS} \propto t^{3/5}$).

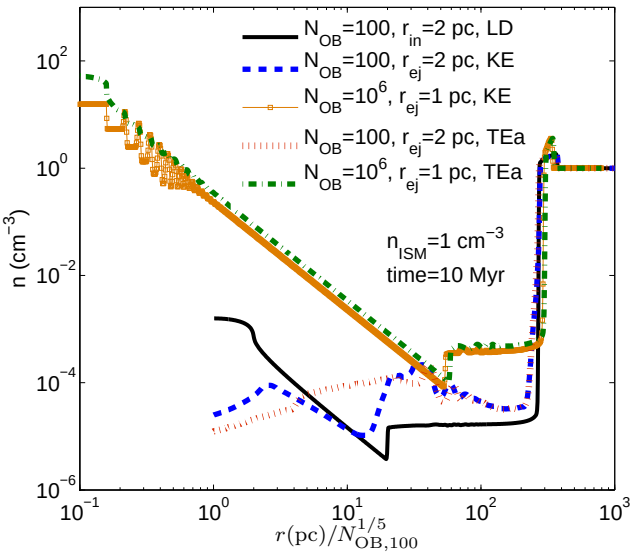

Figure 3. Density profile as a function of normalized radius for luminosity driven (LD), kinetic explosion (KE), and thermal explosion addition (TEa) models. The standard CC85 wind within the bubble appears for the LD model, and for KE and TEa models with $N_{\rm OB} = 10^6$, but not for KE/TEa models with $N_{\rm OB} = 100$. The CC85 wind density using $N_{\rm OB} = 10^6$ is slightly smaller for the KE model compared to the TEa model because density is overwritten (and hence mass is lost) in KE models.

gle blast wave (outer shock radius, $r_{\rm OS} \propto t^{2/5}$) to a continuously driven bubble ($r_{\rm OS} \propto t^{3/5}$; Weaver et al. 1977) for $N_{\rm OB} = 100$ run. The runs with more SNe show such a transition very early on. The dot-dashed line shows the outer shock radius for the KE run using a large ejecta radius violating the criterion in Eq. 1; the outer shock radius is much smaller than expected because energy is overwritten before it energizes the hot bubble (see section 3.1.1). The luminosity driven (LD) and kinetic explosion (KE) models agree only if the ejecta radius is sufficiently small for KE models (we have verified that this constraint also applies to the thermal explosion overwrite [TEo] models); i.e., as long as the condition in section 3.1.1 is satisfied. TEa (thermal explosion addition) runs and LD runs fall on top of each other for both choices of $r_{\rm ej}$ (2, 100 pc). The outer shock radius for runs with $r_{\rm ej} = 100$ pc increase only after a thermalization time (Eq. 5).

4.4 CC85 wind within the bubble

In this section we show that a simple steady wind, as predicted by CC85, exists within the bubble only if the number of SNe is sufficiently large (see section 3.3). Figure 3 shows the density profile as a function of scaled radius for various models. The solid line in Figure 3 shows the density as a function of radius for a luminosity driven (LD) model with $N_{\rm OB} = 100$ and $r_{\rm ej} = 2$ pc. The superwind has a structure identical to the CC85 wind; the sonic point is just beyond the energy injection radius (2 pc). The wind shocks at the termination shock ($r_{\rm TS}$) where the wind ram pressure balances the bubble pressure. The ratio of the termination shock and the outer shock is ≈ 0.07, in good agreement with Eq. 9. For comparison, Figure 3 also shows the density profiles for the kinetic explosion (KE) and thermal explosion addition (TEa) models with the same parameters. While the outer shock radius agree for these runs, the density profiles within the bubble are quite different. The most blatant difference, for runs with $N_{\rm OB} = 100$, is the absence of a CC85 wind in KE and TEa models. In accordance with the discussion in section 3.3, SN shocks do not thermalize within the termination shock for a small number of SNe (see Eqs. 10 & 11) and therefore a smooth CC85 wind is not expected in any model except LD.

Only for a large enough $N_{\rm OB}$ and late enough times does a CC85 wind start to appear within the hot bubble. Figure 3 includes the density profiles for kinetic explosion KE and TEa models using $N_{\rm OB} = 10^6$ (the inner [outer] radius of the computational domain for these runs is 0.5 pc [5 kpc]; $r_{\rm ej} = 1$ pc is chosen to satisfy the constraint in Eq. 1). Clearly, in these cases we see the appearance of the CC85 wind solution within the termination shock because the injected kinetic energy is thermalized. Even for KE runs with $N_{\rm OB} = 10^6$ one can still see the internal shocks due to isolated SNe interacting with the superwind. In agreement with Eq. 9, the ratio $r_{\rm TS}/r_{\rm OS}$ increases with an increasing $N_{\rm OB}$. The density profile for the

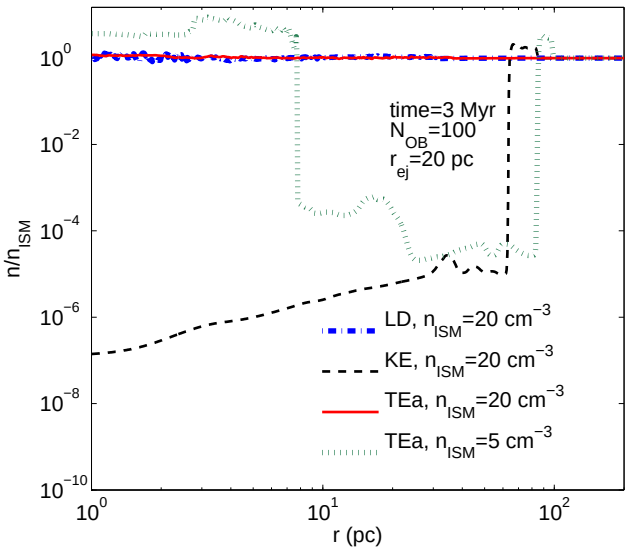

Figure 4. Density as a function of radius for different runs at 3 Myr to show that energy addition totally fizzles out for high ISM density. While TEa and LD models do not show the formation of a hot, dilute bubble for ISM density of 20 cm^{-3}, KE model indeed shows a bubble and a forward shock. Also shown is the density profile for TEa model with a lower density (5 cm^{-3}) ISM; it shows a bubble developing at later times which pushes the shell outwards. The outer shock radius is larger for a lower density ISM because $r_{\rm OS} \propto \rho^{-1/5}$.

KE model using $N_{\rm OB} = 10^5$ is shown by the dotted line in Figure 1. For $N_{\rm OB} = 10^5$ thermalization is less complete as compared to $N_{\rm OB} = 10^6$, but happens within the termination shock. In comparison, a clear termination shock is absent for $N_{\rm OB} = 100$ because the thermalization radius is larger than the termination shock radius (see Eq. 11).

4.5 Effects of radiative cooling

In this section we study the effects of radiative cooling on SNe and SBs. We focus on a few aspects: the fizzling out of thermal feedback in some models in which energy is not injected over a sufficiently small scale; comparison of cooling losses and mechanical energy retained by radiative SNRs and SBs; the influence of magnetic fields and thermal conduction.

4.5.1 Unphysical cooling losses with thermal energy addition

As we mentioned in section 3.2, some models (TEa, LD) in which we *add* SN thermal energy in a dense ISM over a large radius can suffer unphysical catastrophic radiative cooling. In such cases a hot bubble is not even created and SN feedback has no effect, whatsoever. Early SN feedback simulations suffered from this problem because of low resolution.

Figure 4 shows the density profiles at 3 Myr for three of our energy injection models (KE, LD, TEa) with $N_{\rm OB} = 100$ and ISM density of 20 cm^{-3}. The ejecta radius is chosen to be large such that it violates conditions in Eqs. 4 & 7. The figure shows a comparison of the luminosity driven (LD) and thermal explosion addition (TEa) models that fizzle out, and kinetic explosion (KE) model which shows a hot, dilute bubble. Thus our results are in agreement with analytical considerations in section 3.2. The outer shock location for the KE model roughly agrees with the self similar scaling of Weaver et al. (1977) with the luminosity reduced by a factor ≈ 0.35; this is comparable to the fraction of mechanical energy retained by SBs after the outer shock becomes radiative (see section 4.5.4 and the right panel of Fig. 8).

For most runs in Figure 4 we have chosen a rather high density ($n = 20$ cm^{-3}) compared to the critical values in Eqs. 4 & 7. For lower densities (e.g., 5 cm^{-3} for TEa model in Fig. 4) we find that the energy does not couple at early times. Energy injection excites large amplitude sound waves and associated density perturbations, such that at late times the lowest density regions no longer violate Eqs. 4 & 7. After this a hot bubble starts to grow because of energy injection in a dilute medium (see dotted line in Fig. 4), and eventually the outer shock radius agrees with analytic estimates.

4.5.2 SB evolution with cooling

This and later sections, which study the influence of radiative cooling on SBs and SNRs, use the realistic kinetic explosion (KE) model for supernova energy injection with ejecta radius $r_{\rm ej} = 2$ pc. However, we have verified that other models discussed in section 2 give similar results as long as the conditions in section 3 are satisfied.

Spherical adiabatic blast waves, both SNRs and SBs, have shells with finite thickness. An estimate for the shell thickness is obtained by assuming that all the swept-up ISM mass lies in a shell and that the post shock density is 4 times the ISM density for a strong shock; this gives $\Delta r/r_{\rm OS} \approx 1/12$. Of course, the shock transition layer is unresolved in simulations, and in reality is of order the mean free path. The structure of adiabatic blast waves is fairly simple. The density jump at the shock is 4 for a strong shock, and as the shock becomes weaker the density jump decreases and the shell becomes broader. Eventually, the outer shock is so weak that it no longer compresses gas irreversibly, but instead becomes a sound wave with compressions and rarefactions (see Fig. 2 in Tang & Wang 2005).

Since the evolution for isolated SNRs with cooling has been studied in detail in past (e.g., Thornton et al. 1998; hereafter T98), we only highlight the differences between isolated SNRs and SBs. The fundamental difference between the two is that SNRs suffer catastrophic losses just after they become radiative because, unlike in SBs, there is no energy injection after this stage. In SBs the cool (yet dilute), fast SN ejecta periodically thermalizes within the bubble and powers it long after the forward shock becomes radiative. This keeps the radiative forward shock moving (like a pressure-driven snowplow) as long as SNe go off within the hot bubble.

The structure of a radiative shell is quite complex. The shell become radiative when the cooling time of the post-shock gas is shorter than its expansion time (which is of order the age of the blast wave). Moving inward from the upstream ISM, the outer shock transition happens over a mean free path, which is followed by a thin radiative relaxation layer of order the cooling length (see, for example, pp. 226-229 of Shu 1992). The radiative relaxation layer is followed by a dense shell which is separated by a contact discontinuity from the dilute hot bubble. In steady state radiative cooling is concentrated at two unresolved boundary layers, the outer radiative relaxation layer and the inner contact discontinuity where density is high enough and temperature is such that cooling losses are high.

Figure 5 shows the density and temperature structure of the radiative shell for a SB (with $N_{\rm OB} = 10^5$; upper panels) and a SNR ($N_{\rm OB} = 1$; lower panels) for high resolution runs. It clearly shows an outer radiative shock and an inner contact discontinuity. Within the contact discontinuity of the SB ($N_{\rm OB} = 10^5$) is the shocked SN ejecta; as emphasized earlier, a smooth superwind is formed only for a sufficiently large $N_{\rm OB}$ and at late times. Just when the outer shock becomes radiative the coolest/densest part is compressed by high pressure regions sandwiching it (left panels of Fig. 5). After a sound crossing time the post-shock region is roughly isobaric and in the pressure-driven snowplow phase (right panels of Fig. 5).

Unlike SBs, for isolated SNRs there is no energy injection at later times; the pressure in the bubble falls precipitously after the outer shock becomes radiative at ≈0.05 Myr. By ∼ 0.5 Myr the bubble pressure becomes comparable to the ISM pressure, the shell density falls and it becomes momentum conserving with a velocity comparable to the sound speed in the ISM. At even later times (∼ few Myr) the hot bubble just oscillates as a weak acoustic wave.

Figure 6 shows the distribution of radiative losses in the shell and in the bubble (shell is defined as the outermost region where density is above 1.01 times the ISM density; bubble comprises of all the grid points with radius smaller than the inner shell radius) for a superbubble with $N_{\rm OB} = 10^5$. Unlike Figure 5, here we use our standard resolution runs (1024 grid points) because we are running for a much longer time. Results from higher resolution runs match our standard runs, highlighting the fact that the volume integrated cooling is the same even if the radiative relaxation layer and the contact discontinuity are unresolved. The time and volume integrated losses ($\int\int n^2 \Lambda 4\pi r^2 dr dt$) in bubble and shell are sampled appropriately and differentiated in time to obtain their respective cooling rates. As already discussed, cooling is concentrated at the radiative relaxation layer, which is included in the shell, and at the contact discontinuity, part of which is included in the bubble. Consistent with our previous discussion, most radiative losses are concentrated in the shell. Fractional radiative losses in the bubble (concentrated at the contact discontinuity) are $\sim 10^{-4} - 0.3$, which increase with time as the outer shock becomes weaker.

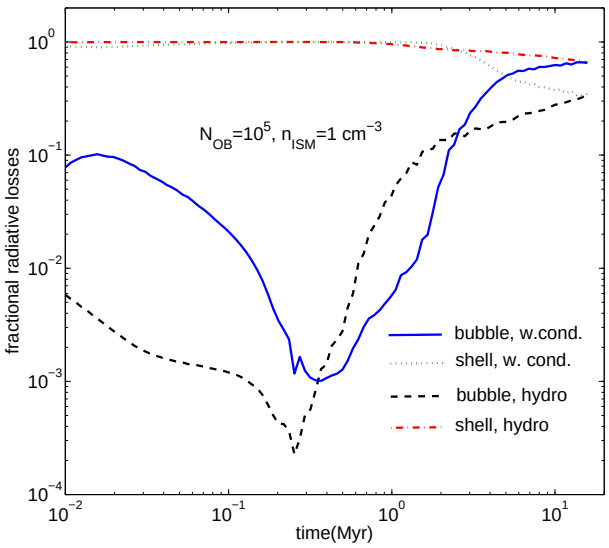

Figure 6. Fractional radiative losses in shell ([shell cooling rate]/[total cooling rate]) and bubble ([bubble cooling rate]/[total cooling rate]) for KE models ($N_{\rm OB} = 10^5$) with and without conduction. Most radiative energy losses happen at the radiative relaxation layer ahead of the dense shell. At late times, as the outer shock weakens, radiative losses in the bubble become more dominant. Bubble is comparatively more radiative (in fact, bubble losses exceed shell losses after 5 Myr) with conduction because of mass loading of the bubble by evaporation from the dense shell. Results from high resolution runs and luminosity driven (LD) models are similar. The minimum in fractional radiative losses corresponds to the time when the outer shock becomes radiative.

4.5.3 Scales in radiative shocks

The structure of a radiative shock is well known (see, e.g., pp. 226-229 in Shu 1992). Applying mass and momentum conservation across the radiative relaxation layer in the shock frame, and assuming the same temperature upstream/downstream of it (see the top right panel of Fig. 5 for different regions of the outer shock) gives $\rho_3/\rho_1 = (u_1/u_3) = (u_1/a_T)^2$ (Eq. 16.36 in Shu 1992), where ρ_3 (ρ_1) is the density downstream (upstream) of the radiative relaxation layer, u_1 (u_3) is the upstream (downstream) velocity in the shock rest frame, and a_T is the isothermal sound speed of upstream ISM (at $T = 10^4$ K below which radiative cooling vanishes). Thus, we expect larger density jump across stronger shocks ($u_1 \gg a_T$). This is evident from the shell density for the two cases ($N_{\rm OB} = 10^5,\ 1$) in Figure 5.

The thickness of the cold, dense shell can be estimated by equating the swept-up ISM mass with the mass in the constant density shell; $\Delta r/r_{\rm OS} \approx (a_T/u_1)^2/3$. This thickness is quite small, with $\Delta r/r_{\rm OS} \approx 0.003$ for a 100 km s^{-1} shock. This estimate agrees with our results in Figure 5, and as predicted, the shell is thicker for a smaller $N_{\rm OB}$ and becomes thicker with time as the shock becomes weaker.

The thickness of radiative relaxation layer can also be

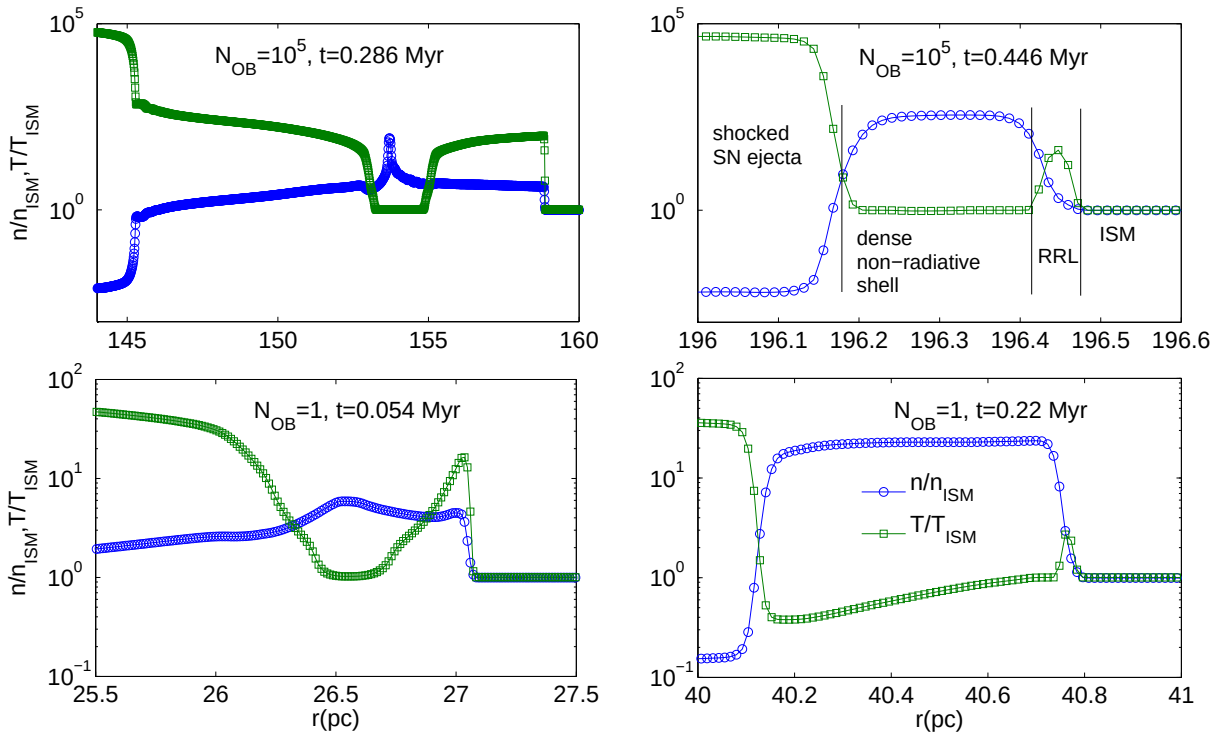

Figure 5. The zoomed-in normalized (with respect to the ISM) density and temperature profiles as a function of radius for high resolution (16384 grid points uniformly spaced from 1 to 200 pc) runs. Top panel: $N_{\rm OB} = 10^5$ run; bottom panel: a single SNR ($N_{\rm OB} = 1$) run. Left panels correspond to a time when the outer shocks just become radiative and the right panels are for later times. Markers represent the grid centers. For a single SNR the temperature in the dense shell is lower than the temperature floor (ISM temperature) because of weakening of the shock and resultant adiabatic losses. Different regions (unshocked ISM, radiative relaxation layer, dense non-radiative shell, and shocked SN ejecta) are marked in the top right panel.

estimated. The size of radiative relaxation layer is $L_{\rm cool}$, such that

$$\int_0^{L_{\rm cool}} \frac{dx}{u} = \int_0^{t_{\rm cool}} dt = t_{\rm cool}, \tag{12}$$

where $u(x)$ is the velocity in the relaxation layer in the shock rest frame (this is the distance behind the outer shock after which the advection time becomes longer than the cooling time). While this equation can only be solved after numerically solving for the structure of the relaxation layer, we can make an order of magnitude estimate. The integral on LHS of Eq. 12 can be estimated as $L_{\rm cool}/\langle u\rangle$, where $\langle u\rangle = a_T/2$ is the geometric mean of the velocity at the front of the relaxation layer ($u_1/4$ for a strong shock) and just downstream of it ($u_3 = a_T^2/u_1$). Similarly, the cooling time $t_{\rm cool}$ in Eq. 12 can be estimated by using a geometric mean of densities across the relaxation layer; i.e., $t_{\rm cool} \approx 1.5kT/(\langle n\rangle\Lambda)$, where $\langle n\rangle = 2(u_1/a_T)n_1$ and we can use the peak of the cooling function for T and Λ. Putting this all together gives

$$L_{\rm cool} \sim a_T \left(\frac{a_T}{u_1}\right) \frac{kT_0}{n_1\Lambda_0}, \tag{13}$$

which is $\sim 10^{-4}$ pc for fiducial numbers, far from being resolved even in our highest resolution runs. While the transition layers (contact discontinuity and radiative relaxation layer) where all our cooling is concentrated are unresolved, we find that the volume integrated quantities such as radiative losses, kinetic/thermal energy in shell/bubble are converged even at our modest (1024 grid points; results are similar even for 256 grid points) resolution.

4.5.4 Energetics of radiative SBs & isolated SNRs

In this section we focus on the energetics of SB shell/bubble and compare it with the results from isolated SNRs. We define the shell to be the outermost region where the density is larger than 1.01 times the ISM density. All gas at radii smaller than the shell inner radius is included in the bubble (this definition is convenient but not very precise as it includes small contribution from the unshocked SN ejecta). Figure 7 shows a comparison of kinetic and thermal energies in bubble and shell as a function of time for a SB driven by 10^5 SNe. The bubble kinetic energy is not included because it is much smaller. Also included is a comparison of the same quantities for the same frequency of SNe that go off independently. The results for multiple isolated SNe are obtained by

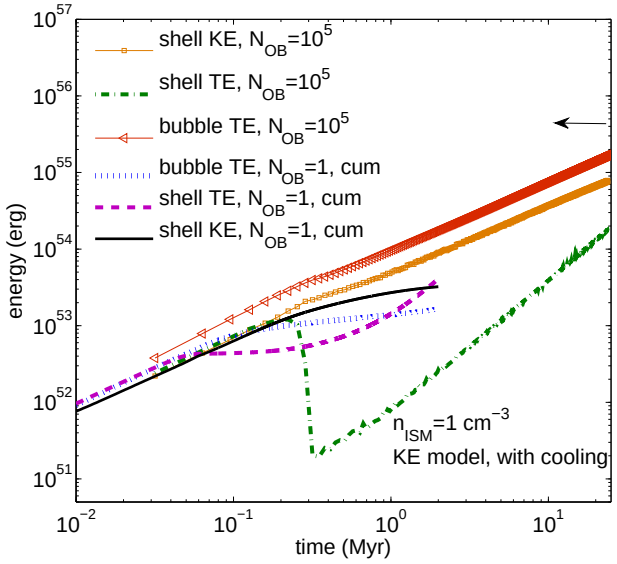

Figure 7. Comparison of kinetic and thermal energies in shell and thermal energy in bubble as a function of time for SBs and an equal number of isolated SNe. Results from an isolated SN run ($N_{\rm OB} = 1$) have been combined cumulatively (see around Eq. 14), assuming that SNe go off independently in the ISM. Pre-radiative phase energetics are similar but isolated SNRs are extremely deficient in mechanical energy (after 1 Myr) as compared to a SB with the same energy input. The arrow on top right shows the bubble thermal energy at the end for an adiabatic SB run. Isolated SN results are only shown till 2 Myr because SNRs become weak sound waves by then.

combining the single SN run at different times. We simply use the data at an interval of $t_{\rm SN}$ (time between individual SNe) and add them to obtain total kinetic/thermal energy in shells and bubbles at a given time. For instance, the thermal energy in bubbles of all independent SNe at time $10t_{\rm SN}$ is obtained by summing up the bubble thermal energy from a single SN ($N_{\rm OB} = 1$) run at $t = 0$, $t_{\rm SN}$, $2t_{\rm SN}$, ..., till $10t_{\rm SN}$. This is equivalent to a cumulative sum over time for a single SN run,

$$E_{\rm cum}(t) = \sum_{i=0}^{i<N} E(it_{\rm SN}) = \frac{1}{t}\int_0^t E(t')dt', \qquad (14)$$

where E stands for, say, bubble thermal energy and N is the number of SNe till time t.

Weaver et al. (1977) have given analytic predictions for energy in different components of SBs: the total energy of the shell is $(6/11)L_{\rm ej}t$ (40% of this is kinetic energy and 60% is thermal) and the thermal energy of the bubble is $(5/11)L_{\rm ej}t$ (kinetic energy of the bubble is negligible). These analytic predictions agree well with our numerical results in the early adiabatic (non-radiative) SB phase in Figure 7.

Figure 7 shows that the SB shell loses most of its thermal energy catastrophically at ≈ 0.25 Myr; the trough in shell thermal energy can be estimated by assuming that all the swept-up mass till then cools to the stable temperature (10^4 K). The thermal energy of the cold shell increases after that as it sweeps up mass from the ISM; this is not a real increase in thermal energy because the newly added material, which was previously part of the ISM, simply becomes a part of the dense shell at the same temperature. The bubble thermal energy and the shell kinetic energy show only a slight decrease in slope after the radiative phase because they are energized by the non-radiative termination (internal) shock(s) driven by SN ejecta. However, there are some losses because of cooling at the contact discontinuity (see Figs. 5 & 6).

The shell kinetic energy and the bubble thermal energy in radiative SB simulations at 20 Myr is roughly half of the values obtained in adiabatic simulations (which agree with analytic predictions). Thus, the mechanical energy retained in bubble and the shell is $\approx 0.35L_{\rm ej}t$. This should be contrasted with the energy evolution in isolated SNRs. The isolated SNR becomes radiative much earlier (≈ 0.05 Myr; when the shell thermal energy shown by dashed line flattens suddenly in Fig. 7) because of a weaker shock compared to a SB. Note that the energies for isolated SNe in Figure 7 are *cumulative sums* over time of a single SN run (see Eq. 14). The bubble thermal energy and shell kinetic energy also drop for an individual SNR after it becomes radiative (albeit not catastrophically, unlike shell thermal energy; see Fig. 3 in T98; this is the pressure-driven snowplow stage) because of cooling at the contact discontinuity and adiabatic losses, and because there is no new energy source (unlike the termination/internal shocks in a SB). The total mechanical energy in the bubble and shell of a single SNR at the beginning of the momentum conserving phase (1 Myr; when bubble pressure is comparable to the ISM pressure) is 10^{50} erg, which is only 10% of the input energy (see Fig. 3 in T98). This agrees with the energy fraction available as mechanical energy of the SNR, as quoted by T98. At this stage the SNR should be considered a part of the ISM as the thermal energy of the swept up ISM becomes larger than the SNR's mechanical energy, and the bubble becomes a weak acoustic wave.

In order to compare isolated SNRs and superbubbles over the cluster lifetime we must extrapolate our cumulative SN energies to 30 Myr. This is also the relevant timescale for preventing large scale inflows from efficiently forming stars. For isolated SNRs the shell kinetic energy + bubble thermal energy is ~7% of the input energy by 2 Myr and only 0.7% when extrapolated to 30 Myr. We should not extrapolate the thermal energy in shell because the rise at late times is due to sweeping up of the ISM into the shell without an increase in temperature. To conclude, isolated SN feedback is much weaker (by a factor ~ 50) as compared to feedback due to SBs over the cluster lifetime.

The left panel of Figure 8 shows the total radiated energy over the whole computational domain as a function of time for an isolated SNR ($N_{\rm OB} = 1$; solid line) and for SBs (dashed lines). The results are qualitatively different for SBs (even for $N_{\rm OB} = 10$) and isolated SNe. While an isolated SN radiates almost all of the input energy (10^{51} erg) over a Myr timescale, SBs radiate a smaller fraction ($0.6 - 0.8$) of their energy even

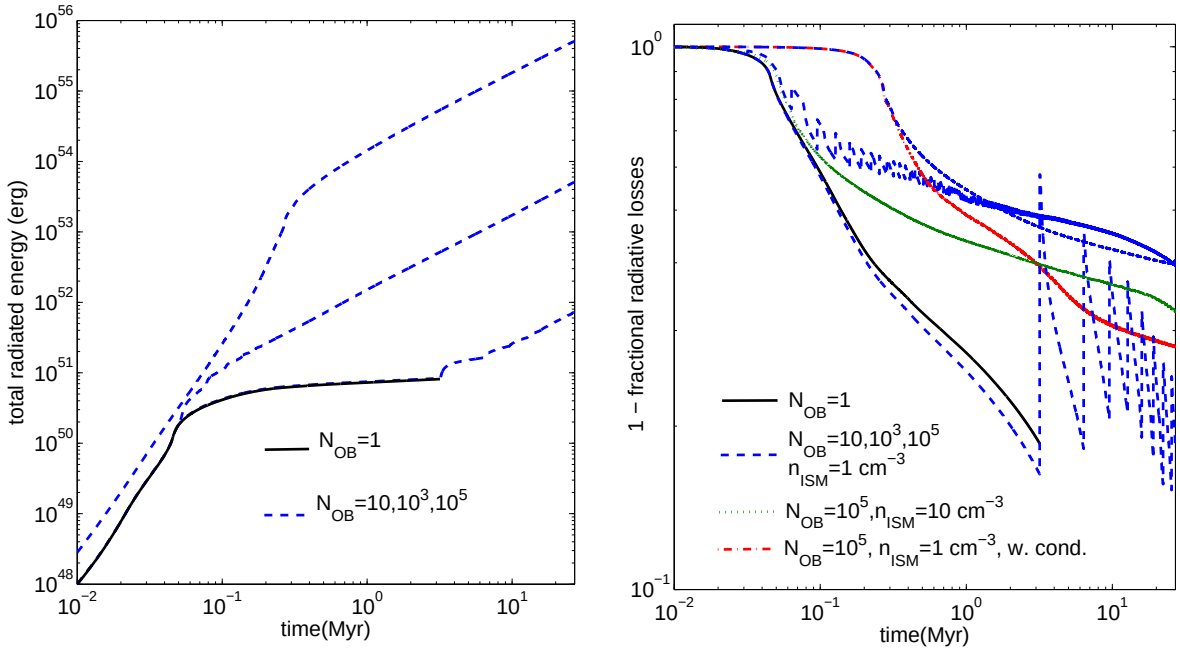

Figure 8. Radiative losses as a function of time for SBs and isolated SNe. Left panel shows total radiated energy as a function of time for an isolated SN run (solid line) and for SB runs (dashed lines) with $N_{\rm OB} = 10,\ 1000,\ 10^5$; larger $N_{\rm OB}$ leads to larger radiative losses because of a higher density and temperature in the radiative relaxation layer (see Fig. 5). The right panel shows fractional cooling losses (1 - [energy radiated]/[input energy]) as a function of time; total energy put in at some time equals number of SNe put in by that time multiplied by 10^{51} erg (the spikes for $N_{\rm OB} = 10,\ 10^3$ in the right panel reflect the discreteness of SN energy input within SBs). All SB runs, including those with conduction and with higher density, show that only a factor of $0.6 - 0.8$ is radiated by 20 Myr (and a factor of $0.2 - 0.4$ is retained as mechanical energy). In contrast, the isolated SN run (solid line) loses most of its energy by this time.

till late times. The runs with smaller $N_{\rm OB}$ and larger density become radiative at an early time as the shock is weaker, but SB runs are qualitatively similar. Unlike isolated SNe, a significant fraction of the input energy in SBs is retained in bubble thermal energy and shell kinetic energy ($0.2 - 0.4$; see Fig. 7). The key reason for the difference between isolated SNe and SBs is that in SBs the non-radiative termination/internal shocks keep the bubble overpressured but isolated SNe, which do not have further energy input after the initial explosion, simply fizzle out soon after they become radiative.

The right panel of Figure 8 shows the fraction of energy retained (1-the fraction radiated) as a function of time for several runs. All SB runs, including a higher density run ($n_{\rm ISM} = 10$ cm^{-3}) and the run with conduction (see section 4.5.5), show the asymptotic fraction of energy retained to be $\gtrsim 0.25$. In contrast, uncorrelated SNe lose 90% of the input energy by few Myr (and almost all of it by 10 Myr). Radiative losses for an isolated SNR at late times ($\gtrsim$ few Myr) are more than the energy input (10^{51} erg); these come at the expense of the thermal energy of the swept-up ISM.

We can compare our results of coincident SNe with the case of multiple SNe distributed over space in a random manner. The two cases presented in Figure 7 represent two extreme limits: spatially coincident SNe in a SB and totally independent SNe. For spatially distributed SNe we expect results somewhere in between these two extremes. Vasiliev et al. (2014) compare the total explosion energy that remains as thermal energy of hot gas in the case of spatially distributed SN explosions. They study the effects of coherent explosions, as defined in Roy et al. (2013), which implies that SNe overlap before they become radiative. If the shell radius of a SNR when it becomes radiative is R_a and the corresponding time scale is t_a, then for a SNe rate density of $\nu_{\rm SN}$, the coherency condition is that $(4\pi/3)\, R_a^3\, t_a\, \nu_{\rm SN} > 1$. Vasiliev et al. (2014) compare the cases in which explosions occur coherently with those in which they do not. They find that a fraction ~ 0.3 of the explosion energy is retained in the gas with temperature $T \geqslant 3 \times 10^6$ K if the explosions occur coherently, and the fraction is $0.02 - 0.2$ if the explosions are incoherent. Our results here for SBs correspond to the coherent case, since $t_{\rm SN}$ is always shorter than the cooling time of the gas in the bubble. Therefore our result of a fraction ~ 0.35 being retained as SB's mechanical energy is consistent with Vasiliev et al. (2014).

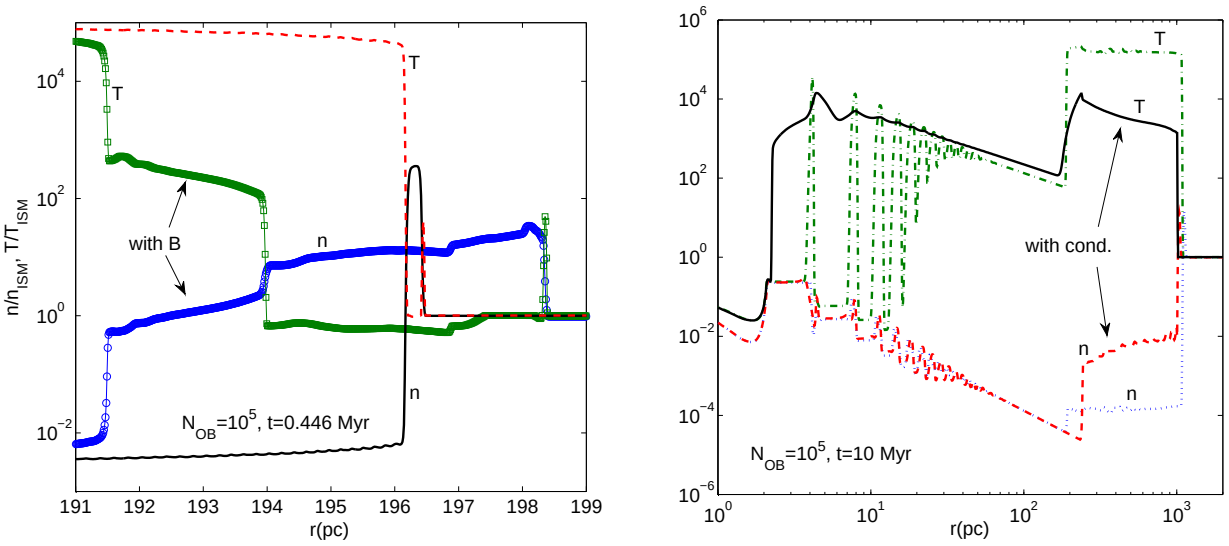

Figure 9. The normalized density and temperature profiles to show the effects of magnetic fields and thermal conduction on SB evolution with cooling. The left panel shows the profiles zoomed in on the outer shock for MHD (initial $\beta = 1$) and hydro runs with 16384 grid points. Magnetic field is enhanced in the shell and the shell is thicker. The right panel shows the profiles for radiative hydro runs with and without thermal conduction (1024 grid points). Thermal conduction evaporates mass from the dense shell and spreads it into the bubble, thereby making it denser and less hot compared to the hydro run. The temperature structure in the internal shocks (within the superwind) is also smoothened out by thermal conduction.

4.5.5 Effects of magnetic fields and thermal conduction

Since the ISM is magnetized, we try to assess the qualitative effects of magnetic fields using an idealized high resolution (16384 grid points) MHD simulation. We assume an azimuthal (ϕ) component of the magnetic field so that only magnetic pressure forces (and no tension) are present. We choose a plasma β (ratio of gas pressure and magnetic pressure) of unity in the ISM, and our SN ejecta is also magnetized with the same value of β. Since the ejecta is dominated by kinetic energy and the bubble is expanding, we do not expect magnetic fields to affect the bubble and the ejecta structure. However, the radiative shell is compressed because of cooling, and due to flux-freezing magnetic pressure is expected to build up in the dense shell. This is indeed what we find in our simulations with magnetic fields. The left panel of Figure 9 shows the density and temperature structure of the radiative outer shock with and without magnetic fields. The key difference between the hydro and MHD runs is that the dense shell in MHD has a lower density and is much broader. This is because magnetic pressure prevents the collapse of the dense shell. The dense shell (194 pc $< r <$ 198 pc in the left panel of Fig. 9) is magnetically dominated with plasma $\beta \sim 0.01$. The MHD run has two contact discontinuities at the boundary of the hot bubble ($r \approx 191.5$ pc), and at $r \approx 194$ pc left (right) of which the plasma is dominated by thermal (magnetic) pressure (see the left panel of Fig. 9).

Another important physical effect, especially in the hot bubble is thermal conduction. We carry out a 1024 resolution hydro run with thermal conduction to study its qualitative influence. However, it is difficult to determine the ISM conductivity in a magnetized (presumably turbulent) plasma. Therefore we use Spitzer value with a suppression factor of 0.2 (see Eq. 11 in Sharma, Parrish, & Quataert 2010). Moreover, since the bubble can become very hot such that the diffusion approximation breaks down, we limit the conductivity to an estimate of the free streaming diffusivity (chosen to be 2.6 $v_t r$ where v_t is the local isothermal sound speed and r is the radius). Thermal conduction is operator split, and implemented fully implicitly through a tridiagonal solver using the code's hydro time step.

Conduction is expected to evaporate matter from the dense shell and deposit it into a conductive layer in the bubble; in steady state the rate of conductive transport of energy from bubble to the shell is balanced by the rate of heat advection from shell to the bubble (Weaver et al. 1977). The outer and termination shock locations are not affected much by conduction. However, the density and temperature structure in the hot bubble is affected significantly. Without conduction the bubble is very hot ($\sim 10^9$ K), but with conduction the temperature drops into the X-ray range ($10^7 - 10^8$ K) and density is higher. This can enhance the X-ray emissivity of SBs; a rough estimate of hard X-ray luminosity ($\int 4\pi r^2 n^2 \Lambda dr$ over the hot bubble) at 10 Myr from the right panel of Figure 9 is few 10^{38} erg s^{-1} (which is ~ 0.003 the energy put in by SNe by that time). Since galactic superwinds are copious X-ray emitters, we expect thermal conduction to be a very important ingredient for explaining observations. Figure 6 confirms that the fraction of radiative losses from the bubble are much

higher with conduction than without conduction because of a higher density.

We emphasize that our treatment of magnetic fields and thermal conduction is extremely simplified. Realistic calculations must be done in three dimensions with tangled magnetic fields and with anisotropic thermal conduction along fields lines. However, we expect the qualitative effects of realistic magnetic fields and thermal conduction to have some semblance with our simplified treatment.

5 CONCLUSIONS & ASTROPHYSICAL IMPLICATIONS

We have obtained several important results in this paper, on both numerical implementation of SN/SB feedback and on differences between isolated SNe and SBs. SBs are a result of spatially and temporally correlated SNe. Since most massive stars are expected to be born in star clusters few 10s of pc in extent (e.g., Larsen 1999), pre-SN stellar winds and first SNe are expected to carve out a low density bubble which by a fraction of Myr encloses the whole star cluster (see Fig. 5). Therefore subsequent SNe happen in the low density bubble and we are in the SB regime of coherent SNe (see Roy et al. 2013; Vasiliev et al. 2014).

Magnificent galactic outflows, such as M82, are powered by multiple super-star clusters and the problem of understanding coalescing SBs is important. Moreover, vertical stratification is important for the acceleration and assimilation of the bubble into the halo. In this paper we consider the idealized smaller scale problem of the behavior of isolated SNRs and multiple coincident SNe within a SB. Some of our most important results are:

- Our most realistic kinetic explosion (KE) models (and for other models in which SN energy is *overwritten*), in which SN energy in kinetic form is overwritten in a small volume, give correct results only if the energy is deposited within a small length scale (see section 3.1.1) because otherwise energy is overwritten without coupling to the ISM. This is true even without considering any radiative losses.
- With cooling, if feedback energy is deposited within a length scale $r_{\rm ej}$ larger than the critical values mentioned in section 3.2, such that the input energy is radiated before it is thermalized, a hot bubble is not formed in the widely used luminosity driven and thermal explosion addition (LD, TEa) models. Thus SN fizzles out at even early stages due to artificially large cooling losses.
- With insufficient resolution and large ISM densities the bubble fizzles out completely in luminosity driven (LD) and thermal explosion addition (TEa) models (in which energy is *added* to the ISM; see section 2) and cannot have any effect on the ISM (see Fig. 4). Early SN feedback simulations failed mainly because of this. However, for a realistic SN (as mimicked by our KE model) a bubble is formed and subsequent SNe occur within the non-radiative bubble, although the outer shock is weak. Another, probably more serious, problem faced by numerical simulations is that SN energy is not typically put in coherently over a small volume in space and within a short interval. Feedback due to SNe in young star clusters is expected to be coherent and much more effective than a similar number of isolated SNe (see Figs. 7, 8). For correlated SNe isolated SN bubbles overlap to form a superbubble which is powered by the non-radiative termination/internal shocks, long after the outer shock becomes radiative. In contrast, an isolated supernova becomes powerless a bit after (~ 1 Myr) the outer shock becomes radiative.
- A smooth CC85 wind within the superbubble is possible only if the number of SNe ($N_{\rm OB}$) over the cluster lifetime is large (i.e., $N_{\rm OB} \gtrsim 10^4$). Only in these cases individual SNe going off inside the superbubble are able to thermalize within the termination shock. This result has implications for modeling the X-ray output, for example, in individual bubbles blown by star clusters and in inner regions of galactic outflows, since the CC85 wind structure is often assumed where it may not be valid.
- Most of the radiative losses come from the unresolved radiative relaxation layer at the outer shock. The fractional radiative losses from the interior region, concentrated at the contact discontinuity between the shocked ISM and the shocked ejecta, varies between $\sim 0.001-0.3$, with larger losses occurring at longer time scales. While these radiative layers are unresolved even in our highest resolution simulations, the volume integrated radiative losses in them converge even for modest resolution.
- Superbubbles can retain a larger fraction of the initial energy of explosions as thermal and kinetic energy of the gas than isolated SNe. Isolated SNe are mixed with the ISM soon after they become radiative; by few Myr they are incapable of affecting the ISM at all. While most energy is radiative away (close to 100%, and not $\sim 90\%$, as is often assumed) for isolated SNe over 10 Myr, a SB can retain a fraction ~ 0.35 (for $n = 1$ cm^{-3}) as bubble thermal energy and shell kinetic energy. This fraction is only weakly affected by a higher ISM density and by thermal conduction (see the right panel of Fig. 8). Thus, SBs are expected to significantly effect even a dense ISM.
- The temperature profile of SBs strongly depend on thermal conduction, whose inclusion can decrease the temperature and thereby enhance the X-ray luminosity. Thermal conduction plays an important role in explaining X-ray emission from galactic superbubbles because very little gas is expected to be in the X-ray emitting regime (10^6-10^8 K) in its absence (see the right panel of Fig. 9).

Our simple one-dimensional simulations show that isolated supernova remnants, owing to large radiative losses, are much weaker feedback agents compared to superbubbles driven by coherently overlapping supernovae. However, detailed three-dimensional calculations, particularly with a realistic distribution of stars in a cluster, and magnetic fields and thermal conduction, are required in order to make quantitative comparisons with observations. This will be done in future.

ACKNOWLEDGEMENTS

PS thanks Ramesh Narayan for useful discussions. PS is partly supported by DST-India grant no. Sr/S2/HEP-048/2012. YS is partly supported by RFBR (project code 12-02-00917).

REFERENCES

Agertz, O., Teyssier, R., & Moore, B. 2011, MNRAS, 410, 1391
Chevalier, R. 1974, MNRAS, 169, 229
Chevalier, R. 1977, Ann. Rev. Astr. Astr., 15, 175
Chevalier, R. A. & Clegg, A. W. 1985, Nature, 317, 44
Chevalier, R. A. & Blondin, J. M. 1995, 444, 312
Cioffi, D. F., McKee, C. F., & Bertschinger, E. 1988, ApJ, 334, 252
Cox, D. P. 1972, ApJ, 178, 159
Creasey P., Theuns, T., Bower, R. G., & Lacey, C. G. 2011, MNRAS, 415, 3706
Creasey, P., Theuns, T., & Bower, R. G. 2013, MNRAS, 429, 1922
Cooper, J. L., Bicknell, G. V., Sutherland, R. S., & Bland-Hawthorn, J. 2008, ApJ, 674, 157
Dubois, Y., Teyssier, R. 2008, A&A, 477, 79
Gerritsen, J. P. E. 1997, PhD Thesis
Gnedin, N. Y. 1998, MNRAS, 297, 407
Guedes, J., Callegari, S., Madau, P., & Mayer, L. 2011, 742, 76
Hayes, J. C. et al. 2006, ApJS, 165, 188
Hopkins, P. F., Quataert, E., & Murray, N. 2011, MNRAS, 417, 950
Hopkins, P. F., Quataert, E., & Murray, N. 2012, MNRAS, 421, 3522
Joung, M. K. R. & Mac Low, M. 2006, ApJ, 653, 1266
Katz, N. 1992, 391, 502
Kay, S. T., Pearce, F. R., Frenk, C. S., & Jenkins, A. 2002, MNRAS, 330, 113
Larsen, S. S. 1999, A&A Supp. Ser., 139, 393
Leisawitz, D., Bash, F. N., & Thaddeus, P. 1989, ApJS, 70, 731
Mac Low, M. & McCray, R. 988, ApJ, 325, 776
Mac Low, M., McCray, R., & Norman, M. L. 1989, ApJ, 337, 141
Mac Low, M. & Ferrara, A. 1999, ApJ, 513, 142
McCray, R. & Kafatos, M. 1987, ApJ, 317, 190
Nath, B. B. & Shchekinov, Y. 2013, ApJL, 777, 12
Navarro, F. F. & White, S. D. M. 1993, MNRAS, 265, 271
Palouš, J., Wünsch, R., Martínez-González, S., Hueyotl-Zahuantitla, F., Silich, S., & Tenorio-Tagle, G. 2013, ApJ, 772, 128
Protegies Zwart, S. F., McMillan, S. L., & Gieles, M. 2010, Ann. Rev. Astr. Astr., 2010, 48, 431
Recchi, S. & Hensler, G. 2013, A&A, 551, 41
Roy, A., Nath, B. B., Sharma, P., & Shchekinov, Y. 2013, MNRAS, 434, 3572
Sharma, P., Parrish, I. J., & Quataert, E. 2010, ApJ, 720, 652
Shu, F. H., The Physics of Astrophysics, vol. II, Gas Dynamics, University Science Books, 1992
Silich, S., Tenorio-Tagle, G., Torres-Campos, A., Munõz-Tuñòn, Monreal-Ibero, A., & Melo, V. 2009, ApJ, 700, 931
Springel, V. & Hernquist, L. 2003, MNRAS, 339, 289
Springel, V. et al. 2005, Nature, 435, 629
Stinson, G., Seth, A., Katz, N., Wadsley, J., Governato, F., & Quinn, T. 2006, MNRAS, 373, 1074
Stone, J. M. & Norman, M. L. 1992, ApJS, 80, 753
Strickland, D. K. & Stevens, I. R. 2000, MNRAS, 314, 511
Strickland, D. K. & Heckman, T. M. 2009, ApJ, 697, 2030
Suchkov, A. A., Balsara, D. S., Heckman, T. M., & Leitherer, C. 1994, ApJ, 430, 511
Sutherland, R. S. & Dopita, M. A. 1993, ApJS, 88, 253
Tang, S. & Wang, Q. D. 2005, ApJ, 628, 205
Tasker, E. J. & Bryan, G. L. 2006, ApJ, 641, 878
Thacker, R. J. & Couchman, H. M. P. 2000, ApJ, 545, 728
Thornton, K., Gaudlitz, M., Janka, H., & Steinmetz, M. 1998, ApJ, 500, 95
Truelove, J. K. & McKee, C. F. 1999, ApJS, 120, 299
Tumlinson, J., Thom, C., Werk, J. K, Prochaska, J. X., Tripp, T. M., Weinberg, D. H., Peeples, M. S., OMeara, J. M., Oppenheimer, B. D., Meiring, J. D., Katz, N. S., Davé, R., Ford, A. B., & Sembach, K. R. 2011, Science, 2011, 334, 948
Vasiliev, E. O., Nath, B. B., Bondarev, R., & Shchekinov, Y. 2014, arXiv:1401.5070
Weaver, R., McCray, R., Castor, J., Shapiro, P., & Moore, R. 1977, ApJ, 218, 377
Zhang, Q., Fall, S. M., & Whitmore, B. C. 2001, ApJ, 561, 727